

SECOND WORKSHOP ON CFD UNCERTAINTY ANALYSIS : RESULTS FROM THE CADYF CODE

A. Hay and D. Pelletier

*Département de Génie Mécanique,
Ecole Polytechnique de Montréal,
Montréal (Québec), CANADA, H3C 3A7*

1 Introduction

This paper introduces, presents and analyses the results from the *Ecole Polytechnique de Montréal* team for the two exercises of the *Second Workshop on Uncertainty Analysis - Lisbon 06*. We assume that the reader knows the details of test cases described in the Workshop proposal. They are not reproduced here for the sake of brevity. Only the boundary conditions will be given since some of them were left for the user to choose. We focus on presenting the CADYF flow solver, the h-adaptive procedure and the numerical error estimation techniques used before providing detailed results for the two cases.

The paper is organized as follows : Section 2 presents the governing equations and their boundary conditions solved by the CADYF code. Section 3 presents the numerical techniques for the flow solver and error estimation. Section 4 provides results for the first test case : a Manufactured Solution that mimics a two-dimensional, steady incompressible turbulent boundary-layer flow. Code Verification as well as the evaluation of the accuracy of the Uncertainty Estimation methods will be performed using the MMS. Finally, the numerical results and their estimated errors are given for the second test case, that is the 2-D steady, incompressible, turbulent flow from the ERCOFTAC Classic Database (Case 30), are discussed in Section 5.

2 Governing equations

2.1 Reynolds-Averaged Navier-Stokes equations

The flows of interest are described by the Reynolds-Averaged Navier-Stokes (RANS) equations. The momentum and mass conservation laws are written as :

$$\rho \mathbf{u} \cdot \nabla \mathbf{u} = -\nabla p + \nabla \cdot (\mu + \mu_T)(\nabla \mathbf{u} + \nabla^T \mathbf{u}) + \mathbf{f} \quad (1)$$

$$\nabla \cdot \mathbf{u} = 0 \quad (2)$$

where ρ is the density, \mathbf{u} the velocity, p the pressure, μ the molecular dynamic viscosity, μ_T the turbulent dynamic viscosity, and \mathbf{f} the volumetric forces.

2.2 The standard $k - \epsilon$ turbulence model

The system is closed by computing the turbulent viscosity using the standard $k - \epsilon$ model. The eddy viscosity is computed from k and ϵ by :

$$\mu_T = \rho C_\mu \frac{k^2}{\epsilon} \quad (3)$$

The transport equations for the two turbulence quantities are :

$$\rho \mathbf{u} \cdot \nabla k = \nabla \cdot \left[\left(\mu + \frac{\mu_T}{\sigma_k} \right) \nabla k \right] + \mu_T \nabla \mathbf{u} : (\nabla \mathbf{u} + \nabla^T \mathbf{u}) - \rho \epsilon + q_k \quad (4)$$

$$\rho \mathbf{u} \cdot \nabla \epsilon = \nabla \cdot \left[\left(\mu + \frac{\mu_T}{\sigma_\epsilon} \right) \nabla \epsilon \right] + C_{\epsilon 1} \mu_T \frac{\epsilon}{k} \nabla \mathbf{u} : (\nabla \mathbf{u} + \nabla^T \mathbf{u}) - C_{\epsilon 2} \rho \frac{\epsilon^2}{k} + q_\epsilon \quad (5)$$

The constants appearing in these equations take the standard values proposed by Launder and Spalding [1] and are given in Table 1. The quantities \mathbf{f} , q_k and q_ϵ will be used as source terms in the MMS

Table 1: Constant of the turbulence model

σ_k	σ_ϵ	$C_{\epsilon 1}$	$C_{\epsilon 2}$	C_μ
1.0	1.3	1.44	1.92	0.09

(see Section 4).

To preserve positivity of the dependent variables (which has several advantages [2, 3]), we work with the logarithmic form of these equations. This can be viewed as using the following change of dependent variables :

$$\mathcal{K} = \ln(k) \quad \text{and} \quad \mathcal{E} = \ln(\epsilon) \quad (6)$$

The transport equations for the logarithmic variables are :

$$\begin{aligned} \rho \mathbf{u} \cdot \nabla \mathcal{K} = \nabla \cdot \left[\left(\mu + \frac{\mu_t}{\sigma_k} \right) \nabla \mathcal{K} \right] + \left(\mu + \frac{\mu_t}{\sigma_k} \right) \nabla \mathcal{K} \cdot \nabla \mathcal{K} \\ + \mu_t e^{-\mathcal{K}} P - \rho^2 C_\mu \frac{e^{\mathcal{K}}}{\mu_t} + q_{\mathcal{K}} \end{aligned} \quad (7)$$

$$\begin{aligned} \rho \mathbf{u} \cdot \nabla \mathcal{E} = \nabla \cdot \left[\left(\mu + \frac{\mu_t}{\sigma_\epsilon} \right) \nabla \mathcal{E} \right] + \left(\mu + \frac{\mu_t}{\sigma_\epsilon} \right) \nabla \mathcal{E} \cdot \nabla \mathcal{E} \\ + \rho C_1 C_\mu e^{\mathcal{K} - \mathcal{E}} P - C_2 \rho e^{\mathcal{E} - \mathcal{K}} + q_{\mathcal{E}} \end{aligned} \quad (8)$$

The production of turbulence P is defined as :

$$P = \nabla \mathbf{u} : [\nabla \mathbf{u} + (\nabla \mathbf{u})^T]$$

Note that equations (7)-(8) are equivalent to the original equations of the turbulence model; only the computational variables are different. Hence, **the turbulence model is unchanged**. The eddy viscosity is given by :

$$\mu_t = \rho C_\mu e^{2\mathcal{K} - \mathcal{E}} \quad (9)$$

2.3 Wall boundary conditions

The standard $k - \epsilon$ turbulence model is not valid when the turbulent Reynolds number is low, as is the case in the near wall regions. Wall functions are used to describe the solution in these regions and will be used for computing the flow over the backward facing step (see Section 5). Thus, the computational wall boundary is taken at a distance d from the physical wall boundary. The region between the two boundaries is the region where the flow is represented by the wall functions. In the remainder, the computational wall boundary will be referred to as the wall and quantities evaluated there will be identified with the subscript w .

We use the two-velocity scale wall functions described by Chabard [4] and Ignat *et al.* [5] and presented in the following paragraphs.

A wall function expresses the value of u^+ , the non-dimensional velocity parallel to the solid wall, as a function of y^+ , the non-dimensional distance from the physical wall :

$$u^+ = \frac{1}{\kappa} \ln(Ey^+) \quad \text{for} \quad y^+ > 10.8 \quad (10)$$

where κ is the Karman constant and E a roughness parameter (for smooth walls $\kappa = 0.42$ and $E = 9.0$). The variables u^+ and y^+ are defined as :

$$y^+ = \frac{\rho d u_k}{\mu} \quad \text{and} \quad u^+ = \frac{u_t}{u_{**}} \quad (11)$$

where $u_t = \mathbf{u} \cdot \hat{\mathbf{t}}$ is the tangential velocity, d is the distance normal to the physical wall and $u_{**} = \sqrt{\tau_w / \rho}$ is a friction velocity. The value of d where the wall function is applied is chosen so that y^+ lies within the range of validity of the wall function (i.e. $30 < y^+ < 300$) [6]. A velocity scale based on the turbulence kinetic energy [4] is computed by :

$$u_k = C_{\mu}^{\frac{1}{4}} k_w^{\frac{1}{2}} = C_{\mu}^{\frac{1}{4}} \exp\left(\frac{\mathcal{K}_w}{2}\right) \quad (12)$$

The boundary conditions associated with the governing equations are as follows :

- flow boundary condition in the tangential direction : the tangential force exerted by the fluid on the wall is a prescribed function of the tangential velocity (mixed or Robin boundary condition). Using the two-velocity scale wall function leads to a linear relationship between the wall shear stress τ_w and u_t .

$$[(\boldsymbol{\tau} \cdot \hat{\mathbf{n}}) \cdot \hat{\mathbf{t}}]_{wall} = \tau_w = \rho u_k u_{**} = \frac{\rho u_k}{\frac{1}{\kappa} \ln(E \frac{\rho d u_k}{\mu})} u_t \quad (13)$$

- flow boundary condition in the normal direction : the normal velocity is set to zero.

$$\mathbf{u} \cdot \hat{\mathbf{n}} = 0 \quad (14)$$

- boundary condition for \mathcal{K} : The \mathcal{K} -equation is solved with a zero normal flux boundary condition. This condition arises from the fact that the wall shear stress is assumed constant in the wall functions region (i.e. $0 < y^+ < 300$) [6]. This Neumann condition is required to compute the distribution of u_k along the wall.

$$\left(\mu + \frac{\mu_t}{\sigma_k}\right) \nabla \mathcal{K} \cdot \hat{\mathbf{n}} = 0 \quad (15)$$

- boundary condition for \mathcal{E} : The boundary condition for the logarithm of ϵ is the logarithm of the usual Dirichlet boundary condition for the turbulence kinetic energy dissipation rate at the wall in which the velocity scaled u_k is used instead of u_{**} .

$$\mathcal{E} = \ln\left(\frac{u_k^3}{\kappa d}\right) \quad (16)$$

3 Numerical Techniques

3.1 General Presentation

The RANS equations (Eqs. (1)- (2)) and the logarithmic form of the turbulence equations (Eqs. (7)-(8)) are solved by a finite element method. The weak forms of the equations are obtained by multiplying them by a set of test functions and integrating by parts them over the domain to yield residual equations. They are reduced to zero by making them orthogonal to the set of test functions [7]. We use a mixed or velocity-pressure formulation in which a Lagrange multiplier (the pressure in the fluid) is used to enforce the incompressibility constraint. The velocity and the logarithmic turbulence variables are discretized using 6-noded quadratic elements. Fluid pressure is discretized by piecewise linear continuous functions (element $P_2 - P_1$). For high Reynolds number, the equations are dominated by convection so that the standard Galerkin discretization may lead to non-physical oscillations and convergence difficulties. Hence, some form of upwinding is required. This is done by using the Streamline Upwind/Petrov-Galerkin (SUPG) stabilized formulation initially proposed by Brooks and Hughes [8] and further improved by Ilinca *at al* [9]. The resulting finite element method is formally third order accurate for all the variables except the pressure which is only second order accurate. Hence, the stresses $-pI + (\mu + \mu_T)(\nabla \mathbf{u} + \nabla^T \mathbf{u})$ and the diffusion of \mathcal{K} and \mathcal{E} are formally second order accurate. However, the stabilization formulation locally introduces small amount of artificial numerical diffusion which may reduce the accuracy of the standard finite element formulation.

The discretization of the equations leads to a system of non-linear algebraic equations which are linearized by Newton's method. All linear algebraic systems are solved using a skyline direct solver.

The global system of equations are solved in a partly segregated manner as illustrated in figure 1. This algorithm has been derived by rewriting the equations for k and ϵ in block triangular form using the eddy viscosity definition as presented in Ref. [3, 10]. Global iterates are performed for

- | |
|--|
| (0) given initial solutions : $\mathbf{u}_0, \mathcal{K}_0, \mathcal{E}_0$ |
| (1) compute μ_{t_i} from \mathcal{K}_i and \mathcal{E}_i |
| (2) for μ_{t_i} given |
| (2.1) solve momentum-continuity |
| (2.2) solve the \mathcal{K} -equation |
| (2.3) solve the \mathcal{E} -equation |
| (2.4) update μ_t and go to step (2) |

Figure 1: Solution algorithm

the momentum-continuity and turbulence equations. Sub-iterations of steps (2.2)-(2.4) of turbulence transport equations are also used to accelerate the overall convergence of the iterative process (see Refs. [11, 2, 10, 12] for more details).

3.2 Error Estimation and adaptive procedure

The accuracy of the finite-element approximation can be directly related to the local mesh size. An adaptive remeshing procedure is employed to improve the accuracy, by refining the mesh in regions of high error in the flow and turbulence variables. Regions targeted for refinement are identified by the Zhu-Zienkiewicz (ZZ) error estimator [13, 14] which evaluates estimates of elemental error norms. It has been shown to be asymptotically exact using a proper measure (norm) of the error for a class of elliptic problem. The error estimator is based on local projections of discontinuous quantities onto a local continuous polynomial basis. For example, since the $P_2 - P_1$ element uses a piecewise quadratic basis for the velocity, the stress tensor is linear and discontinuous. By projecting it onto a continuous polynomial basis, we can derive an error estimate defined as the difference between the finite-element stresses and their projections. Thus, the elemental error can only be measured in the so-called energy

norm (or a mathematically equivalent such as the H^1 semi-norm). As a consequence, the following norms are considered in the present work :

$$\text{H1U} : \|\mathbf{u}\|_{H^1} = \sqrt{\int_{\Omega} (\nabla u \cdot \nabla u + \nabla v \cdot \nabla v) d\Omega} \quad (17)$$

$$\text{H1P} : \|p\|_{H^1} = \sqrt{\int_{\Omega} \nabla p \cdot \nabla p d\Omega} \quad (18)$$

$$\text{EVK} : \|\mathcal{K}\|_{eqv} = \sqrt{\int_{\Omega} \nabla \mathcal{K} \cdot \nabla \mathcal{K} d\Omega} \quad (19)$$

$$\text{EVE} : \|\mathcal{E}\|_{eqv} = \sqrt{\int_{\Omega} \nabla \mathcal{E} \cdot \nabla \mathcal{E} d\Omega} \quad (20)$$

$$\text{EVM} : \|\mu_t\|_{eqv} = \sqrt{\int_{\Omega} \nabla \mu_t \cdot \nabla \mu_t d\Omega} \quad (21)$$

The error norms are obtained by replacing the quantity by its exact or estimated error. For example, the true elemental error is :

$$\|e_p\|_{H^1}^{\text{exa}} = \sqrt{\int_{\Omega} (\nabla p_{\text{exa}} - \nabla p_h) \cdot (\nabla p_{\text{exa}} - \nabla p_h) d\Omega}$$

while the ZZ estimate is obtained by evaluating :

$$\|e_p\|_{H^1}^{\text{ZZ}} = \sqrt{\int_{\Omega} (\nabla p_{\text{ZZ}} - \nabla p_h) \cdot (\nabla p_{\text{ZZ}} - \nabla p_h) d\Omega}$$

The above expressions yield global quantities when integration is performed on the whole domain Ω . Elemental errors and estimates result from integration over a given element volume Ω_k . Once error estimates are obtained for all variables (flow and turbulence variables), an optimal mesh size distribution is determined using the asymptotic convergence rate of the finite-element method and the principle of equidistribution of the error. The optimal mesh is generated to redistribute the mesh sizes so that each element has the same contribution to the norm of the total error. This is performed in an iterative fashion, beginning with a coarse mesh and producing a sequence of meshes which reduce the error by a constant factor over that of the previous mesh. The mesh characteristics (element size) are derived separately for each dependent variable using the norms previously defined. The minimum element size predicted by each of the dependent variable is selected on a given element. The computational domain is then remeshed using an advancing front technique. Details of this adaptive remeshing procedure may be found in the literature [15, 16, 17]. Note that an additional error estimate for the eddy viscosity is also constructed since slowly varying fields of \mathcal{K} and \mathcal{E} can result in rapid variation of μ_t . This is important to the success of adaptation in turbulent flows since the eddy viscosity is the sole mechanism for transfer of momentum and turbulent kinetic energy by turbulent fluctuations [18, 3].

The ZZ error estimator belongs to the family of post-processing techniques (or least-squares-based recovery techniques). The essence of the ZZ error estimator is to use the difference between the post-processed field and the original finite element solution as a measure of the error. Obviously, the error estimation is crucially dependent on the order of accuracy of the post-processed solution. It is worth noting that a very much improved process, named the Super-convergent Patch Recovery (SPR) [13, 14, 19], has been developed and yields super-convergent values of solutions. Similar

post-processed procedures have been developed in the wake of the SPR. Wiberg *et al.* made further improvements by requiring that the recovered quantities satisfy the equilibrium equation and/or boundary conditions [20]. These techniques yield asymptotically exact local (or point wise) estimate of the true error. Thus, asymptotically exact error estimates are obtained in any norm. All these procedures are similar to the ZZ projection. However, they assume some super-convergence property of the finite element : the post-processing is made by fitting a higher order polynomial expansion, by the least squares method, to the finite element solutions at super-convergent points over a patch. A mathematical proof that a recovery-based estimator yields an asymptotically exact estimate of the error, if the super-convergent property holds, can be found in Ref. [21]. However, it should be stressed that super-convergence only occurs in very special circumstances and generally speaking only for simple problems and some FE discretization. No super-convergence property has ever been observed for the Navier-Stokes equations (even for regular grids and laminar flows). In the cases where there is no super-convergence property, the asymptotic exactness of the derived error estimators can no longer be proved formally.

In practice, however, recovery-based estimators perform surprisingly well in cases where no super-convergent property holds if a proper norm of the error is used. The reason behind this robustness is not fully understood but appears to depend on the fact that the finite element derivatives are discontinuous from one element to the next (the projected solution being continuous). This explains why the ZZ estimator can only yield elemental error estimates in the norm of the derivatives (H^1 semi-norm) and not in the L_2 norm of the variable. As will be shown and already illustrated in the literature [18, 16], the ZZ estimator is ideally suited for driving mesh adaptation. However, this feature constitutes a serious weakness if one is focusing on quantitative assessment of point-wise numerical accuracy since the ZZ estimator does not provide point-wise information.

To remedy the situation and achieve point-wise error estimates, we proceed as follows. The meshes are generated by adaptive remeshing driven by the ZZ estimator. Point-wise error estimates are obtained by a separate and different reconstruction. We use an L_2 least squares approach (i.e. project the solution rather than its derivatives). We approximate the exact field over an element by a polynomial of degree $k + 2$ where k is the degree of the finite element basis functions. A point-wise error estimate is computed by taking the difference between the L_2 elemental reconstruction and the finite element solution in the appropriate element containing the point of interest (see Ref. [22] for details).

4 Test Case 1 : Manufactured Solution

4.1 Manufactured solution and Boundary conditions

The manufactured solution is thoroughly described in Ref. [23]. It mimics the near-wall behavior of a two-dimensional, steady incompressible turbulent boundary-layer. The near-wall behaviour of all the specified quantities is similar to what is observed in near-wall turbulent flows.

The standard two-equation $k-\epsilon$ model is supposed to be valid only in fully-turbulent regions. The damping functions of the two one-equation models suggest that the present manufactured solution is not fully-turbulent close to the bottom [23]. Nevertheless, the application of the MMS being a purely mathematical exercise, the present MS can be used for the standard $k-\epsilon$ model as well. However, at the bottom of the computational domain, ($y = 0$), the source term of the ϵ transport equation tends to infinity, due to the behaviour of the dissipation term. In the present context of a manufactured solution, this will lead to a transport equation for ϵ driven by the forcing source term in the "near-wall" region. Hence, its usefulness for Calculation Verification may be questionable.

The computational variables for the turbulence model are the logarithms of k and ϵ . As stated

earlier, the original turbulence model is unchanged, only the computational variables are different. However, with such a formulation, the manufactured k and ϵ of any manufactured solution must not value zero in any part of the computational domain since the logarithm function would be singular. As a consequence, the original manufactured solution presented in Ref. [23] was slightly modified by adding small constants α_k and α_ϵ to the MS :

$$k = k_{max}\eta_\nu^2 e^{1-\eta_\nu^2} + \alpha_k \quad (22)$$

$$\epsilon = 0.36 \frac{k_{max}^2}{\nu_{max}} e^{-\eta_\nu^2} + \alpha_\epsilon \quad (23)$$

A trade-off must be made when choosing the values of the two constants. They must be large enough to avoid any numerical problem originating from the logarithm function. And, they must be chosen so that the differences with the original manufactured solution to be negligible (including the manufactured eddy-viscosity field). Following these observations, we choose :

$$\alpha_k = 10^{-5} \quad ; \quad \alpha_\epsilon = 10^{-3} \quad (24)$$

Even though no formal proof is available, we believe that these modifications of the manufactured turbulent kinetic energy and dissipation rate have no significant influence on the manufactured fields. Furthermore, the verification exercises are not changed at all. For example, we examine the value of the manufactured eddy-viscosity at the wall which originally is zero. Using the expressions from Eqs. (22) - (23) and the values from (24), the manufactured eddy-viscosity at the wall is :

$$(\mu_t)_w = \rho C_\mu \frac{\alpha_k^2}{0.036 + \alpha_\epsilon} = \frac{9}{3.7} 10^{-10} \quad (25)$$

Hence, the value of the manufactured eddy-viscosity at the wall is negligible compared to the molecular viscosity.

We now examine the boundary conditions for this manufactured problem. They must be set using the exact solution. The following boundary conditions are typical of such problems. Both Dirichlet and Neumann boundary conditions are applied for the verification exercise to be complete :

<u>Inflow boundary</u>	$U_h = U(y)$ $V_h = V(y)$ $k_h = k(y)$ $\epsilon_h = \epsilon(y)$	<u>Upper boundary</u>	$U_h = U(x)$ $V_h = V(x)$ $k_h = k(x)$ $\epsilon_h = \epsilon(x)$
<u>Outflow boundary</u>	$k_h = k(y)$ $\epsilon_h = \epsilon(y)$ $(\sigma_h \cdot \mathbf{n}) \cdot \hat{\mathbf{i}} = -p(y) + 2(\mu + \mu_T(y))U_{,x}(y)$ $(\sigma_h \cdot \mathbf{n}) \cdot \hat{\mathbf{j}} = (\mu + \mu_T(y))(U_{,y}(y) + V_{,x}(y))$	<u>Lower boundary</u>	$U_h = U(x)$ $V_h = V(x)$ $k_h = k(x)$ $\epsilon_h = \epsilon(x)$

Where subscript h denotes the discrete solution.

4.2 Numerical results

Seven grid adaptation cycles have been performed. Figure 2 shows the last adapted grid which contains 108 665 nodes. It is typical of adapted meshes for boundary layer flow problems as expected. Extensive refinement is observed in the near-wall region. Several bands of refinement can also be identified which correspond to regions of rapid variation in velocity, \mathcal{K} , \mathcal{E} and μ_t .

Figures 3 and 4 shows the evolution of the global error norms defined by Eqs. (17) - (21) (true and estimated) with the adaptive cycles. The corresponding efficiency indices (ratio of estimated error over the exact error) are presented in figure 5. As explained previously, since the turbulence variables

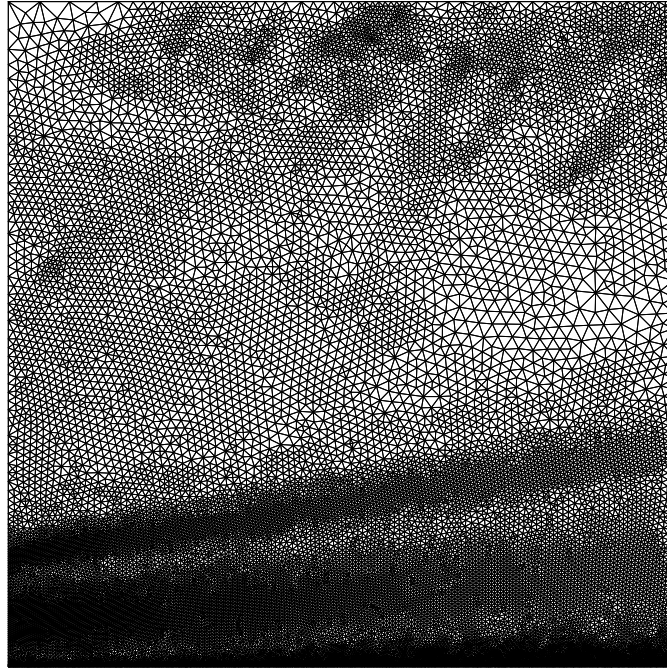


Figure 2: Adapted mesh for the manufactured solution

are solved in logarithmic form, adaptation is performed on ZZ reconstructions for the logarithmic variables \mathcal{K} and \mathcal{E} (note that their orders of magnitude are significantly different from those of the original variables). As can be seen, the errors decrease with mesh refinement and the numerical solution converges towards the exact solution. Furthermore, the error estimates approach the true errors with mesh refinement. This indicates that adaptation improves the accuracy of both the solution and the error estimator. In order to evaluate more precisely the accuracy of the estimated errors,

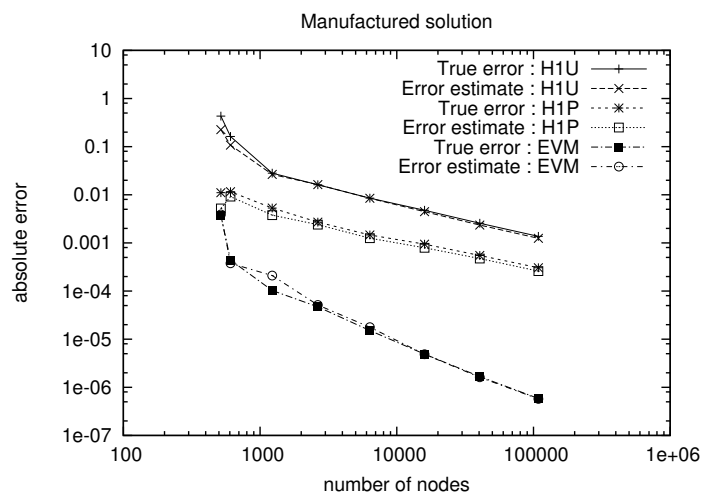


Figure 3: Evolution of global error norms with adaptive cycles (1)

table 2 provides the values of the global error norms along with their associated efficiency indices computed on the last adapted mesh. As can be seen, all the efficiency indices are very close to one indicating that the ZZ error estimator performs well.

As part of the Code Verification exercise, we now look at the observed orders of convergence for

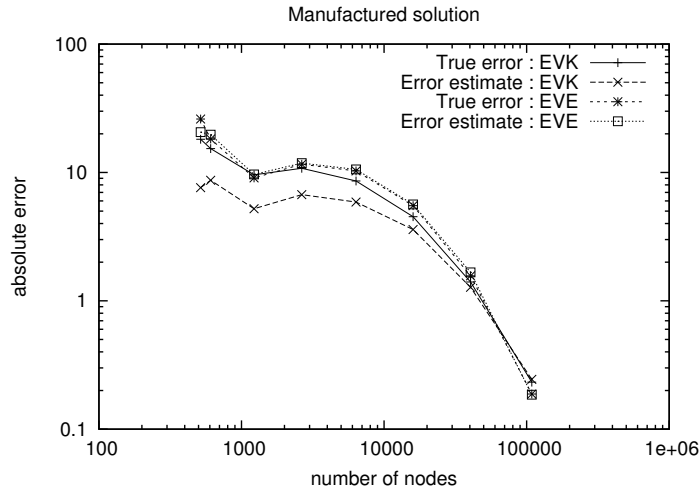


Figure 4: Evolution of global error norms with adaptive cycles (2)

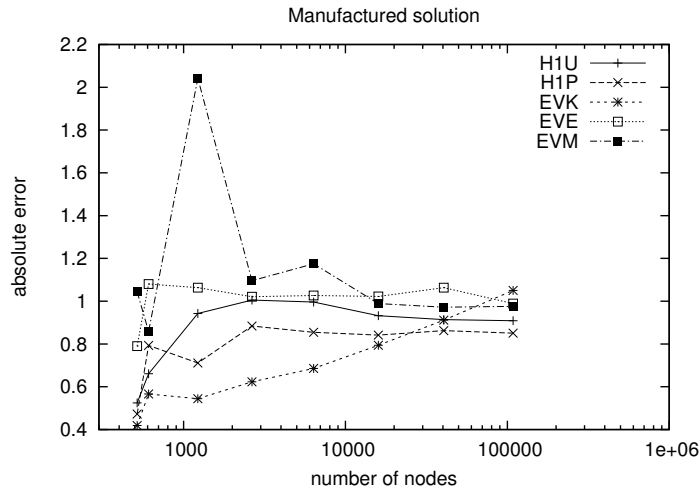


Figure 5: Evolution of efficiency indices with adaptive cycles

	Exact	Estimated	Efficiency index
H1U	$1.370 \cdot 10^{-3}$	$1.245 \cdot 10^{-3}$	0.909
H1P	$3.044 \cdot 10^{-4}$	$2.590 \cdot 10^{-4}$	0.851
EQK	$2.325 \cdot 10^{-1}$	$2.441 \cdot 10^{-1}$	1.050
EQE	$1.878 \cdot 10^{-1}$	$1.857 \cdot 10^{-1}$	0.989
EQM	$5.879 \cdot 10^{-7}$	$5.739 \cdot 10^{-7}$	0.976

Table 2: Global error norms

the dependent variables. These observed orders are computed from the exact global error norms on two different meshes. However, the use of the adaptive procedure leads to a difficulty in the evaluation of these orders since the refinement ratio between two consecutive grids in the adaptive process is clearly not uniform over the computational domain (except if the asymptotic range has been reached and the error is already equidistributed for all variables). A coarser grid with a refinement ratio of 2 is

easily obtained by the advancing front method by setting the coarser mesh size to $\delta_H = \sqrt{2}\delta_h$. This is equivalent to a coarsening by $\sqrt{2}$ in each direction so that the number of grid points is halved at each cycles of mesh coarsening. This is easily done by our mesh generator but can not be enforced exactly everywhere for technical reasons. However, the refinement ratio between these two meshes is nearly constant over the domain which is better suited for the evaluation of the observed orders of accuracy from the global error norms. The observed rates of convergence are given in table 3. Without the stabilization terms, the theoretical orders of accuracy of the standard Galerkin FEM should be 2 for all norms but the HIP for which the order should be 1. However, the stabilization formulation locally introduces small amount of artificial numerical diffusion which can degrade the accuracy. As can be seen from table 3, the effect of the stabilization terms is less pronounced on the pressure than on the other variables (\mathbf{u} , \mathcal{K} , \mathcal{E}). This was expected since the pressure discretization is second order accurate while the others variables discretization is third order accurate, thus the influence of the first order numerical diffusion from the stabilization terms should be less important on p . From these results,

H1U	H1P	EQK	EQE	EQM
1.273	0.902	2.318	2.768	2.122

Table 3: Observed orders of convergence in global exact error norms

we can deduce the observed orders of convergence of the variables which are given in table 4 along with their corresponding theoretical orders of convergence. The differences between the theory and what is observed arises from the loss of accuracy due to numerical diffusion techniques for dealing with high Reynolds number problem.

	\mathbf{u}	p	\mathcal{K}	\mathcal{E}	μ_t
theoretical	3.000	2.000	3.000	3.000	3.000
observed	2.273	1.902	3.318	3.768	3.122

Table 4: Orders of convergence of variables

We now focus our attention to the evaluation of the accuracy of the error estimation technique for an integral quantity : the friction resistance R_f on the wall. Taking $\rho U_{\text{ref}}^2 L_{\text{ref}}$ as a reference force, the friction resistance is computed as follows :

$$R_f = \frac{1}{\rho U_{\text{ref}}^2 L_{\text{ref}}} \int_{\Gamma_w} \tau \cdot \hat{\mathbf{n}} \cdot \mathbf{e}_y \, d\Gamma \quad (26)$$

Figure 6 shows the evolution of R_f with adaptive cycles. As can be seen, grid convergence of R_f is achieved rapidly by the adaptive strategy. Table 5 gives values of the friction coefficient Eq. (6) and its errors on the last adaptive grid. As can be seen, the relative exact error on R_f is small ($2.68864 \cdot 10^{-5}$) and the estimated error is relatively close to the exact error with an efficiency index of 0.581. From this we conclude that the error estimation method for integral quantity successfully computes the order of magnitude of the exact error but does not provide even one significant digit. However, it is a fairly accurate error prediction for a high Reynolds turbulent flow.

Friction Coefficient	Exact Error	Estimated Error	Efficiency index
$0.312938 \cdot 10^{-5}$	$0.841375 \cdot 10^{-10}$	$0.488755 \cdot 10^{-10}$	0.581

Table 5: Results for the friction coefficient

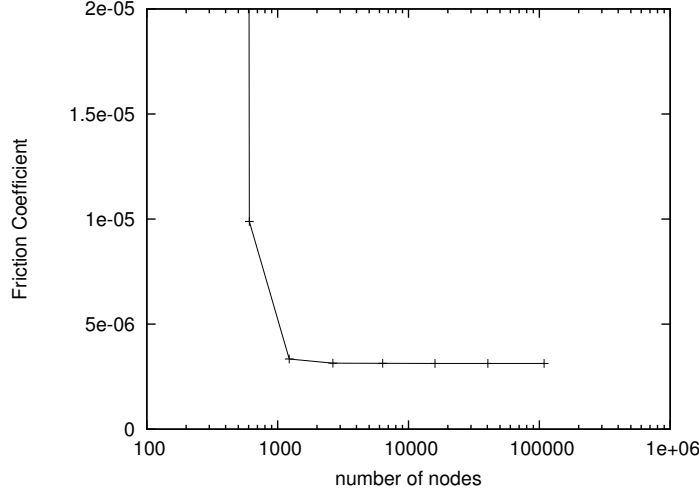


Figure 6: Evolution of R_f with adaptive cycles

Finally, the accuracy of the error estimation technique for local flow quantities is examined. The coordinates of the three local points under consideration are : Point 1 (0.600,0.001), Point 2 (0.750,0.002) and Point 3 (0.900,0.200). At these locations, we study the values of the velocity components (U and V), the pressure coefficient C_p , the eddy-viscosity μ_t and their associated errors. Note that here, the pressure coefficient is defined as :

$$C_p = \frac{p}{\rho U_{\text{ref}}^2} \quad (27)$$

The results are collected in table 6. All the values have been checked for grid convergence with

Local point	Variables	Value	Exact Error	Estimated Error	Efficiency index
1	U	$0.752228 \cdot 10^{-2}$	$0.138221 \cdot 10^{-6}$	$0.100532 \cdot 10^{-6}$	0.727
	V	$0.626501 \cdot 10^{-5}$	$0.362070 \cdot 10^{-8}$	$0.149948 \cdot 10^{-7}$	4.141
	C_p	$0.961490 \cdot 10^{-2}$	$0.100520 \cdot 10^{-8}$	$0.386091 \cdot 10^{-8}$	3.841
	μ_t	$0.748136 \cdot 10^{-9}$	$0.114963 \cdot 10^{-11}$	$0.778382 \cdot 10^{-12}$	0.677
2	U	$0.120354 \cdot 10^{-1}$	$0.229121 \cdot 10^{-6}$	$0.167990 \cdot 10^{-6}$	0.733
	V	$0.159042 \cdot 10^{-4}$	$0.142939 \cdot 10^{-6}$	$0.116034 \cdot 10^{-6}$	0.812
	C_p	$0.191728 \cdot 10^{-1}$	$0.145184 \cdot 10^{-7}$	$0.790371 \cdot 10^{-8}$	0.544
	μ_t	$0.209155 \cdot 10^{-8}$	$0.432803 \cdot 10^{-12}$	$0.676875 \cdot 10^{-12}$	1.564
3	U	$0.791275 \cdot 10^{+0}$	$0.358949 \cdot 10^{-6}$	$0.903074 \cdot 10^{-7}$	0.252
	V	$0.770422 \cdot 10^{-1}$	$0.538351 \cdot 10^{-6}$	$0.628828 \cdot 10^{-6}$	1.168
	C_p	$0.161486 \cdot 10^{-1}$	$0.131497 \cdot 10^{-6}$	$0.310776 \cdot 10^{-6}$	2.363
	μ_t	$0.676005 \cdot 10^{-4}$	$0.111044 \cdot 10^{-9}$	$0.189889 \cdot 10^{-8}$	17.100

Table 6: Results for local flow quantities

a convergence behaviour similar to the one observed for the friction resistance (see figure 6). The maximum exact relative error is found on the value of μ_t at point 2 ($0.898750 \cdot 10^{-2}$) and in general the finite element solution reproduces the exact solution with more than four or five significant digits.

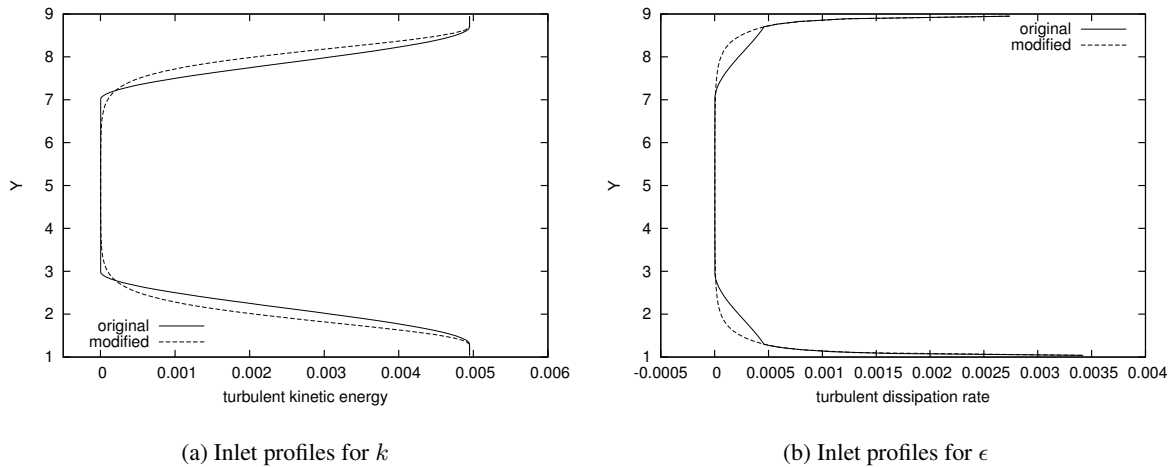


Figure 7: Inlet profiles for the turbulence variables

The error estimate based on the Wiberg solution reconstruction over an element predicts the order of magnitude of the exact error for all the values but the one of μ_t at point 3. In general, the accuracy of the error estimation is similar to the one observed for the integral quantity. Deriving an average efficiency index is a non-trivial task. Simple arithmetic averaging can lead to misleading results. We have opted to normalize all efficiency indices by using their inverse when greater than one. This is acceptable since an index value of ξ is equivalent to one of $\frac{1}{\xi}$ the difference being that one of them indicates overestimation while the other one expresses underestimation. Neither is preferable. This approach leads to a mean efficiency index of 0.498. These results are satisfactory in terms of accurate error prediction for this class of problem and typical of what was observed previously. However, since the error is not fully reproduced, it would be useful to derive safety coefficients to compute error bands in the spirit of the Grid Convergence Index [24]. Finding the safety factors would require a large number of test cases for achieving error bands that are correct in ninety five percent of the cases. The present results are promising and bode well for deriving a mono-grid error band procedure.

5 Test Case 2 : Backward Facing Step

For this test case, the boundary conditions along walls are prescribed using wall functions. At the inlet, Dirichlet boundary conditions are applied and at the outlet we prescribed homogeneous Neumann boundary conditions. The inlet profiles for all variables are defined using experimental data and mathematical treatments to ensure the continuity of both the variables and their derivatives. The original inlet profiles for the turbulent variables are plotted in figure 7. As stated, these profiles are constructed in a piecewise manner to obtain C^1 continuous functions as required by most numerical techniques. However, the logarithms of these C^1 continuous functions are no longer C^1 continuous. This may lead to numerical problems for our code. Hence, we slightly modified the inlet profiles. The background experimental data are unchanged but the piecewise mathematical treatment for obtaining the profiles is done so that our computational variables (the logarithms of the turbulent variables) is C^1 continuous. The resulting inlet profiles thus obtained are plotted in figure 7. We believe that the modification of the profiles will only have minor influence on the computed solution since the physics behind these modified profiles is the same than for the original ones. Only, the mathematical assembly is different.

Seven grid adaptation cycles have been performed. Figure 8 shows the last adapted grid which contain 55 776 nodes. An close-up view of the adapted mesh around the step is also provided in figure 9. It is similar to adapted meshes obtained for the flow over a backward facing step as studied experimentally by Kim [25] and the one studied experimentally by Vogel *et al* [12]. Similarly to

previous wall-bounded flow grids, the refinement has been performed intensively in the near-wall region. Different bands of refinement can also be identified which correspond to regions of rapid variation in velocity, \mathcal{K} , \mathcal{E} and μ_t .

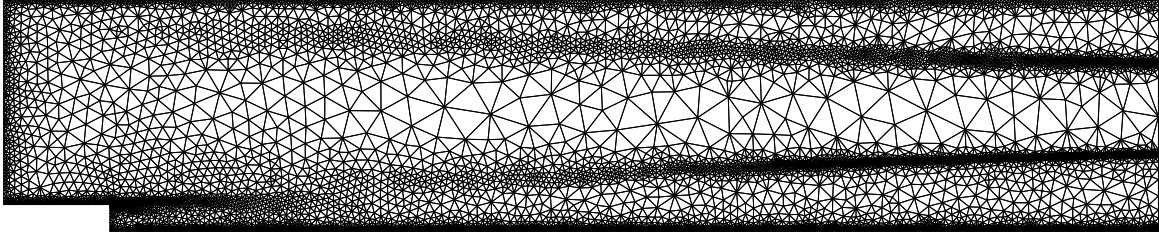


Figure 8: Adapted mesh for the backward facing step

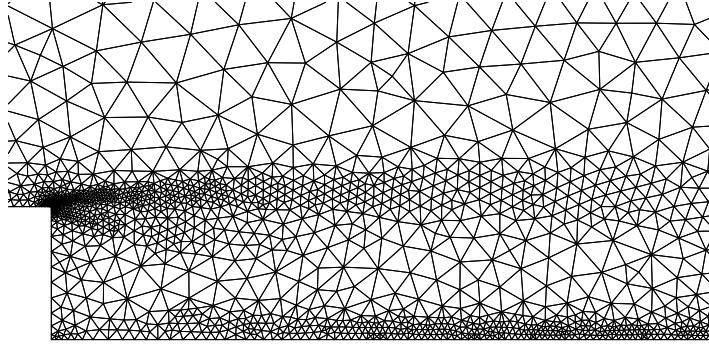


Figure 9: Inside view of the adapted mesh around the step

Before proceeding with any analysis of the results, we must check that the non-dimensional wall distance chosen for each wall lies in the interval of validity imposed by the wall functions. That is, it is required that y^+ be less than 300 and greater than 30 but preferably as close to 30 as possible. Figure 10 gives the evolution of y^+ with adaptive cycles for each wall. As can be seen, the wall distances converge with the adaptive cycles. And, for the last adapted grid, the above condition is satisfied everywhere except near the corner singularity.

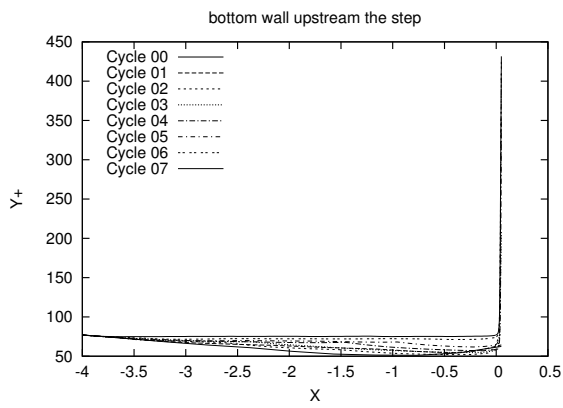
We first examine the result for the recirculation length. Figure 11 shows the evolution of the computed recirculation length with adaptive cycles. As can be seen, convergence is achieved. The value of the non-dimensional recirculation length computed on the last adapted mesh is 5.446699. The evaluation of the discretization error is 0.102065.

We now examine several integral quantities : the friction resistance R_f on the bottom and top walls and the pressure resistance R_p on the bottom wall. Taking $\rho U_{\text{ref}}^2 L_{\text{ref}}$ as a reference force, the friction resistance is computed from Eq. (26) and the pressure resistance as follows :

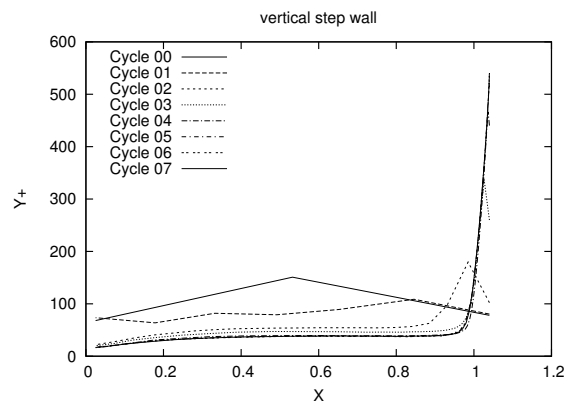
$$R_p = \frac{1}{\rho U_{\text{ref}}^2 L_{\text{ref}}} \int_{\Gamma_w} -(p - p_{\text{outlet}}) \hat{\mathbf{n}} \cdot \mathbf{e}_y \, d\Gamma \quad (28)$$

Table 7 gives the numerical values of the coefficients and their estimated errors on the last adaptive grid.

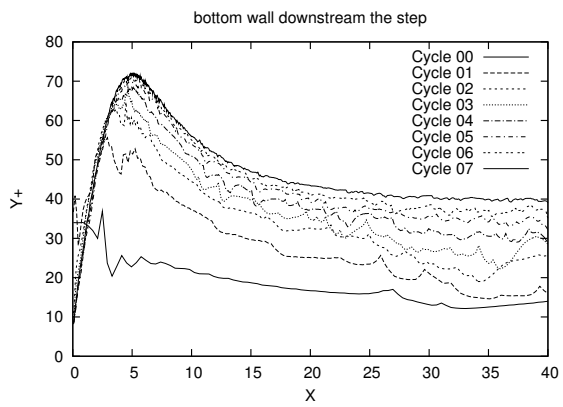
Finally, the error on local flow quantities is examined. The coordinates of the three points under consideration are : Point 1 (0.0,1.1), Point 2 (1.0,0.1) and Point 3 (4.0,0.1). At these locations, we



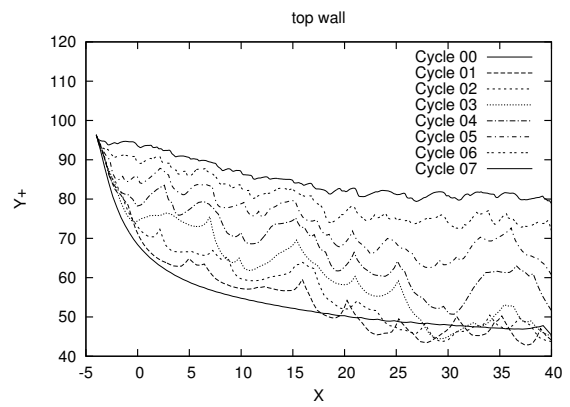
(a)



(b)



(c)



(d)

Figure 10: Evolution of y_+ with adaptive cycles

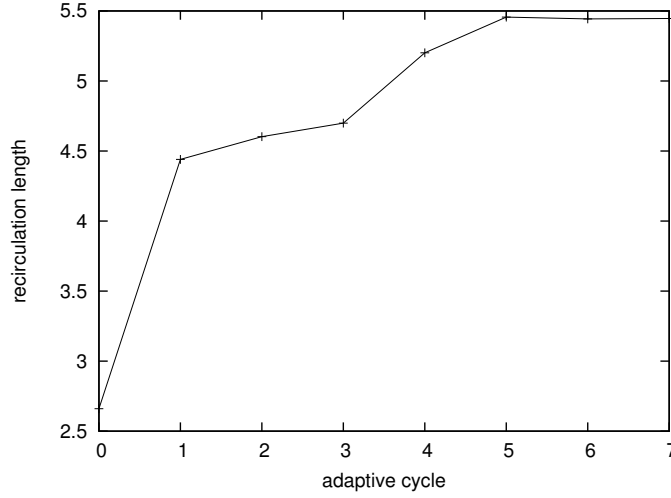


Figure 11: Evolution of recirculation length with adaptive cycles

	R_f on the bottom wall	R_f on the top wall	R_p on the bottom wall
Value	$0.526499 \cdot 10^{-01}$	$0.672544 \cdot 10^{-01}$	$0.119342 \cdot 10^{+00}$
Estimated Error	$0.993600 \cdot 10^{-02}$	$0.253363 \cdot 10^{-01}$	$0.223481 \cdot 10^{-01}$

Table 7: Results for the resistance coefficients

consider the values of the velocity components (U and V), the pressure coefficient C_p , the eddy-viscosity μ_t and their errors. Note that here, the pressure coefficient is defined as :

$$C_p = \frac{p - p_{\text{outlet}}}{1/2\rho U_{\text{ref}}^2}$$

The results are collected in table 8. All the values have been checked for grid convergence with a convergence behaviour similar to the one observed for the recirculation length (see figure 11). The maximum estimated relative error is found on the value of μ_t at point 2 ($0.898476 \cdot 10^{-2}$). Generally speaking the error estimates appear sharp in that they are small enough to provide hints that we have achieved 4 to 5 significant digits in predictions.

6 Concluding remarks

This paper has presented the results for the two test cases proposed for the *Second Workshop on Uncertainty Analysis - Lisbon 06* from the *Ecole Polytechnique de Montréal* team. The CADYF-FEM flow solver, the h-adaptive procedure and the numerical error estimation techniques used has been detailed. The manufactured problem provides a Verification of the code in the sense of Roache [24] and provides reference information about the accuracy and reliability of the estimation error procedures used. All the results requested for the Workshop have been given.

References

- [1] B. E. Launder and J. Spalding. The numerical computation of turbulent flows. *Computer Methods in Applied Mechanics and Engineering*, pages 269–289, 1974.

Local point	Variables	Value	Estimated Error
1	U	$+0.647700 \cdot 10^{+00}$	$0.396496 \cdot 10^{-04}$
	V	$+0.289958 \cdot 10^{-01}$	$0.102193 \cdot 10^{-03}$
	C_p	$-0.133953 \cdot 10^{+00}$	$0.339351 \cdot 10^{-04}$
	μ_t	$+0.171898 \cdot 10^{-02}$	$0.314743 \cdot 10^{-06}$
2	U	$-0.944773 \cdot 10^{-01}$	$0.371167 \cdot 10^{-04}$
	V	$+0.721732 \cdot 10^{-02}$	$0.110560 \cdot 10^{-04}$
	C_p	$-0.237365 \cdot 10^{+00}$	$0.226732 \cdot 10^{-05}$
	μ_t	$+0.195559 \cdot 10^{-02}$	$0.175705 \cdot 10^{-04}$
3	U	$-0.125582 \cdot 10^{+00}$	$0.109521 \cdot 10^{-04}$
	V	$-0.608819 \cdot 10^{-02}$	$0.796328 \cdot 10^{-06}$
	C_p	$-0.139171 \cdot 10^{+00}$	$0.484284 \cdot 10^{-05}$
	μ_t	$+0.612614 \cdot 10^{-02}$	$0.185213 \cdot 10^{-04}$

Table 8: Results for local flow quantities

- [2] F. Ilinca and D. Pelletier. Positivity preservation and adaptive solution for the $k - \epsilon$ model of turbulence. *AIAA Journal*, 36(1):44–51, 1998.
- [3] F. Ilinca, J.-F. Héту, and D. Pelletier. Adaptive remeshing for the $k - \epsilon$ model of turbulence. *Computers and Fluids*, 27(3):291–310, 1998.
- [4] J.-P. Chabard. Projet N3S - manuel de la version 3, 1991. Tech. Rep. EDF HE-41/91.30B, Electricité de France.
- [5] L. Ignat, D. Pelletier, and F. Ilinca. Adaptive computation of turbulent forced convection. *Numerical Heat Transfer, Part A*, 34:847–871, 1998.
- [6] J.A. Schetz. *Boundary Layer Analysis*. Prentice Hall, 1993.
- [7] J. N. Reddy. *An introduction to the finite element method*. McGraw-Hill, 1984.
- [8] A. N. Brooks and T. J. R. Hughes. Streamline upwind/petrov-galerkin formulations for convection dominated flows with particular emphasis on the incompressible navier-stokes equations. *Computer Methods in Applied Mechanics and Engineering*, 32:199–259, 1982.
- [9] F. Ilinca, J.-F. Héту, and D. Pelletier. On stabilized finite element formulations for incompressible advective-diffusive transport and fluid flow problems. *Computer Methods in Applied Mechanics and Engineering*, 188(1):235–257, 2000.
- [10] F. Ilinca and J.-F. Héту. Finite element solution of three-dimensional turbulent flows applied to mold-filling problems. *International Journal for Numerical Methods in Fluids*, 34:729–750, 2000.
- [11] F. Ilinca. *Méthodes d’éléments finis adaptatives pour les écoulements turbulents*. PhD thesis, École Polytechnique de Montréal, 1996.
- [12] D. Lacasse, É. Turgeon, and D. Pelletier. On the judicious use of the $k - \epsilon$ model, wall functions and adaptivity. In *39th AIAA Aerospace Sciences Meeting and Exhibit*, Reno, NV, Jan. 2001. AIAA Paper 2001-0882.

- [13] O. C. Zienkiewicz and J. Z. Zhu. The superconvergent patch recovery and *a posteriori* error estimates. Part 1: The recovery technique. *International Journal for Numerical Methods in Engineering*, 33:1331–1364, 1992.
- [14] O. C. Zienkiewicz and J. Z. Zhu. The superconvergent patch recovery and *a posteriori* error estimates. Part 2: Error estimates and adaptivity. *International Journal for Numerical Methods in Engineering*, 33:1365–1382, 1992.
- [15] J. Peraire, M. Vahdati, K. Morgan, and O.C. Ziekiewicz. Adaptive remeshing for compressible flow computations. *Journal of Computational Physics*, 72(2):449–466, 1987.
- [16] D. Pelletier. Adaptive finite element computations of complex flows. *International Journal for Numerical Methods in Fluids*, 31:189–202, 1999.
- [17] É. Turgeon, D. Pelletier, and J. Borggaard. A continuous sensitivity equation approach to optimal design in mixed convection. In *33rd AIAA Thermophysics Conference*, Norfolk, VA, Jun.-Jul. 1999. AIAA Paper 99-3625.
- [18] D. Pelletier and F. Ilinca. Adaptive remeshing for the $k - \epsilon$ model of turbulence. *AIAA Journal*, 35(4):640–646, 1997.
- [19] O. C. Zienkiewicz and J. Z. Zhu. The superconvergent patch recovery (spr) and adaptive finite element refinement. *Computer Methods in Applied Mechanics and Engineering*, 101:207–224, 1992.
- [20] N.-E. Wiberg and F. Abdulwahab. Patch recovery on superconvergent derivatives and equilibrium. *International Journal for Numerical Methods in Fluids*, 36:2703–2724, 1993.
- [21] M. Ainsworth and T. J. Oden. *A posteriori error estimation in finite element analysis*. John Wiley & Sons, New York, 2000.
- [22] X. D. Li and N.-E. Wiberg. A posteriori error estimate by element patch post-processing, adaptive analysis in energy and l_2 norms. *Computers and Structures*, 53(4):907–919, 1994.
- [23] L. Eça, M. Hoekstra, A. Hay, and D. Pelletier. A manufactured solution for a two-dimensional steady wall-bounded incompressible turbulent flow. In *7th World Congress on Computational Mechanics, Accomplishments and Challenges in Verification & Validation*, Los Angeles, July 2006.
- [24] P. J. Roache. *Verification and Validation in Computational Science and Engineering*. Hermosa Publishers, Albuquerque, NM, 1998.
- [25] É. Turgeon, D. Pelletier, S. Etienne, and J. Borggaard. Sensitivity and uncertainty analysis for turbulent flows. In *44th AIAA Aerospace Sciences Meeting and Exhibit*, Reno, NV, January 2002. AIAA Paper 2002-0985.